

Geophysical Research Letters®



RESEARCH LETTER

10.1029/2024GL109283

Special Collection:

Land-atmosphere coupling:
measurement, modelling and
analysis

Disaggregating the Carbon Exchange of Degrading Permafrost Peatlands Using Bayesian Deep Learning

Norbert Pirk¹ , Kristoffer Aalstad¹ , Erik Schytt Mannerfelt¹ , François Clayer² , Heleen de Wit² , Casper T. Christiansen³, Inge Althuizen⁴ , Hanna Lee⁵ , and Sebastian Westermann¹ 

¹Department of Geosciences, University of Oslo, Oslo, Norway, ²Norwegian Institute for Water Research (NIVA), Oslo, Norway, ³University of Copenhagen, Copenhagen, Denmark, ⁴NORCE Norwegian Research Centre, Bergen, Norway, ⁵Norwegian University of Science and Technology, Trondheim, Norway

Key Points:

- Eddy covariance fluxes are disaggregated for different surfaces using Bayesian neural networks to derive uncertainty-aware carbon balances
- While palsa areas have a near-zero annual methane balance, the fens and ponds that form upon palsa degradation emit large amounts of methane
- Fens compensate for methane emissions with strong annual CO₂ sinks, while ponds appear as strong, yet uncertain, CO₂ emission hotspots

Supporting Information:

Supporting Information may be found in the online version of this article.

Correspondence to:

N. Pirk,
norbert.pirk@geo.uio.no

Citation:

Pirk, N., Aalstad, K., Mannerfelt, E. S., Clayer, F., de Wit, H., Christiansen, C. T., et al. (2024). Disaggregating the carbon exchange of degrading permafrost peatlands using Bayesian deep learning. *Geophysical Research Letters*, *51*, e2024GL109283. <https://doi.org/10.1029/2024GL109283>

Received 14 MAR 2024

Accepted 1 MAY 2024

© 2024. The Author(s).

This is an open access article under the terms of the [Creative Commons Attribution-NonCommercial-NoDerivs License](https://creativecommons.org/licenses/by/4.0/), which permits use and distribution in any medium, provided the original work is properly cited, the use is non-commercial and no modifications or adaptations are made.

Abstract Extensive regions in the permafrost zone are projected to become climatically unsuitable to sustain permafrost peatlands over the next century, suggesting transformations in these landscapes that can leave large amounts of permafrost carbon vulnerable to post-thaw decomposition. We present 3 years of eddy covariance measurements of CH₄ and CO₂ fluxes from the degrading permafrost peatland Iškoras in Northern Norway, which we disaggregate into separate fluxes of palsa, pond, and fen areas using information provided by the dynamic flux footprint in a novel ensemble-based Bayesian deep neural network framework. The 3-year mean CO₂-equivalent flux is estimated to be 106 gCO₂ m⁻² yr⁻¹ for palsas, 1,780 gCO₂ m⁻² yr⁻¹ for ponds, and -31 gCO₂ m⁻² yr⁻¹ for fens, indicating that possible palsa degradation to thermokarst ponds would strengthen the local greenhouse gas forcing by a factor of about 17, while transformation into fens would slightly reduce the current local greenhouse gas forcing.

Plain Language Summary Arctic and sub-arctic regions on the southern border of the permafrost zone often feature peatlands with a patchy surface of peat mounds, thaw ponds, and surrounding fens. As the permafrost underneath peat mounds thaws, these areas transform and can change their emission or uptake of greenhouse gases like CO₂ and methane. Assessing this gas exchange on the patchy surface is difficult because our measurement techniques cannot directly observe the variability in space and time. We collected 3 years of gas exchange measurements at a Norwegian permafrost peatland and developed a new method using a collection of uncertainty-aware neural networks to predict the greenhouse gas exchange of different surface types. Our work suggests that large amounts of methane are emitted by ponds and fens, while the elevated peat mounds have almost no methane emissions. For CO₂, we see that ponds are strong emitters, while fens take up substantial amounts as their vegetation absorbs this gas. We are still unsure when the peat mounds will collapse and if they turn into ponds or fens, but we can say that pond formation would give a 17 fold increase in greenhouse gas emissions, while fen formation would slightly reduce today's emissions of permafrost peatlands.

1. Introduction

Permafrost peatlands are considered to be some of the most dynamic and rapidly changing ecosystems in the permafrost zone (Olefeldt et al., 2016). These ecosystems cover large areas in often harsh and inaccessible arctic regions, playing an important role in the global carbon cycle as they have historically accumulated large amounts of soil organic carbon which is vulnerable to microbial re-mobilization upon climate warming (Oechel et al., 2000; Schuur et al., 2015). The characteristic palsa peat mounds—elevated by excess ground ice in the permafrost—are increasingly subject to thawing and degradation, resulting in thermokarst pond or wetland formation (Borge et al., 2017; Grosse et al., 2013; Luoto & Seppälä, 2003; Martin et al., 2021; Sannel & Kuhry, 2011). While irreversible palsa collapse is widely anticipated in large regions of the pan-Arctic over the coming century (Aas et al., 2019), the dynamics of the degradation as well as the state and fate of their carbon stocks remain elusive.

The emission and uptake of the greenhouse gases carbon dioxide (CO₂) and methane (CH₄) is associated with a stark heterogeneity as a result of the patchy surface cover consisting of different plant and microbial communities, which can inform possible future trends of land-atmosphere interactions through space-for-time substitutions (e.g., Jiao et al., 2023). While moist or inundated areas typically feature microbes with anaerobic metabolisms producing CH₄, drier areas are dominated by aerobic soil respiration that produces CO₂ and may even consume

considerable amounts of atmospheric CH₄ (Voigt et al., 2019, 2023). Thermokarst ponds are typically supersaturated in dissolved CO₂ and CH₄, and emissions can be associated with diffusive fluxes (Matveev et al., 2016; Serikova et al., 2019) as well as gas ebullition (Burke et al., 2019; Walter et al., 2006). The pathways of gas production, consumption, dissolution, transport, and emission in permafrost peatlands depend on a complex interplay of biogeochemical processes that are influenced by a plethora of interacting environmental factors, including soil, surface, and atmospheric conditions. As a result, CO₂ and CH₄ exchange can vary tremendously on small spatio-temporal scales, which complicates the representative (unbiased) quantification of the greenhouse gas budgets of permafrost peatlands based on sparse flux measurements. Consequently, the quantification of the greenhouse gas balances not only reflects the ecosystem in its environmental setting, but can also depend strongly on the method used to estimate them.

Using the manual chamber technique Nykänen et al. (2003) estimated that palsa surfaces with shrub vegetation in northern Finland were sinks of (atmospheric) carbon, whereas palsa surfaces with sparse vegetation were carbon sources. In their study, the annual emissions of CH₄ ranged from 1.0 gC m⁻² yr⁻¹ on top of the palsas to 24.7 gC m⁻² yr⁻¹ at the palsa margins. However, the manual chamber technique only allows for sporadic spatio-temporal sampling, and unwanted disturbances by the manual deployment of the chamber are inevitable (Kutzbach et al., 2007), adding uncertainty to the estimated annual budgets. Year-round automatic chamber measurements in the Stordalen permafrost peatland in Sweden indicate CO₂ sinks and CH₄ sources in the mire, with a net carbon balance of -13 gC m⁻² yr⁻¹ for palsa areas and -91 gC m⁻² yr⁻¹ for fen areas (Holmes et al., 2022). While such estimates are derived from near-continuous flux measurements, the long-term presence of the chamber base can disturb the ecosystem as it locally increases air temperature similar to an open-top chamber (Frei et al., 2020) and a fair number of automatic chambers are required to obtain spatially representative estimates. Moreover, potentially important flux hotspots in wetlands can be unsuitable for the operation of an automatic flux chamber, because water levels can be too high or too variable. Measurements with the micro-meteorological eddy covariance (EC) technique (Baldocchi, 2020) in a nearby palsa-dominated area in Stordalen indicate a sink of CO₂ with an annual balance amounting to between -20 and -95 gC m⁻² yr⁻¹ across the years, as well as relatively stable CH₄ emissions of between 18 and 22 gC m⁻² yr⁻¹ (Christensen et al., 2012). The anemometer and gas analyzer needed for EC measurements can in principle be operated year-round, but unfavorable micro-meteorological conditions due to a lack of stationarity or weak turbulent mixing will inevitably cause gaps in the flux time series. As these gaps tend to occur systematically, for example, in very stable conditions during nights or wintertime, gap-filling is needed to avoid biased seasonal or annual flux budgets. While EC measurements are widely regarded as the most accurate flux measurements on the landscape scale, it must be noted that the flux footprint of the measurements changes continuously depending on the wind conditions. So unless the ecosystem around the flux tower can be considered spatially homogeneous, the flux time series will contain confounding effects of both spatial and temporal variability. A possible indication of this effect can be seen in the EC measurements from a Siberian palsa mire reported by Olchev et al. (2022), where CH₄ fluxes show alternating uptake and release fluxes, possibly as a result of the surface heterogeneity. A simple flux footprint disaggregation by wind sector can be a viable option in special cases (Griebel et al., 2016; Pirk et al., 2023), but a generally accepted disaggregation method remains lacking.

Levy et al. (2020) present a Bayesian method to infer spatial heterogeneity in surface fluxes from individual control variables at an EC tower using the information provided by the temporally changing footprint. As the surface fluxes of CO₂ and CH₄ result from a complex interplay of biogeochemical processes, the more advanced parameterizations encoded in process-based land-surface models (Lawrence et al., 2019; Qiu et al., 2018) or non-linear data-driven models such as deep neural networks (Krizhevsky et al., 2012; LeCun et al., 2015; Murphy, 2023) can be appropriate options. Neural networks can in principle approximate any functional relationship between inputs (predictors) and outputs (fluxes) (Hornik et al., 1989), but their parameters (weights of the network edges and bias terms of the nodes) are less interpretable than those used in process-based models (Rudin, 2019). In practice, finding a suitable network architecture for a given problem can be challenging and training these networks may require vast amounts of data for complex relationships. To alleviate these challenges, one may incorporate Bayesian inference into the training process of the network by treating the model parameters as random variables with probability distributions representing their uncertainty. Such Bayesian neural networks (BNNs) produce uncertainty-aware outputs and—while being an old concept (MacKay, 2003; Neal, 1996)—are becoming increasingly popular in machine learning where uncertainty awareness is becoming a vital

consideration (Ghahramani, 2015). In Earth system science, BNNs remain a relatively unexplored topic (Clare et al., 2022; Lopez-Gomez et al., 2022), despite the popularity of deep learning (Reichstein et al., 2019).

Here, we present 3 years of EC fluxes of CO₂ and CH₄ collected at a permafrost peatland in northern Norway. We develop a new flux disaggregation method using ensemble-based Bayesian deep learning with predictors from in-situ measurements and satellite remote sensing to estimate uncertainty-aware fluxes separately for palsa, pond, and fen areas. We use historic aerial photography as well as a modern drone-based survey of terrain changes to characterize the permafrost degradation and inform future scenarios for the carbon balance of permafrost peatlands through a space-for-time substitution.

2. Materials and Methods

2.1. Site Description and Surface Characterization

Our study is conducted at the I skoras permafrost peatland (69.34°N, 25.30°E, 380 m a.s.l., shown in Figure S1 in Supporting Information S1), which is located on the Finnmarksvidda mountain plateau in northern Norway. The climate here is classified as subarctic or polar, with a mean annual air temperature of -1.2°C and a mean annual precipitation of 417 mm for the period 1991–2020 (measured at weather station SN97251 approximately 15 km north of I skoras). The years of our study period feature no outliers in mean annual air temperature and total annual precipitation, and are relatively similar to the long-term mean conditions. The site lies just above the current tree line with mountain birch trees, and features typical upland tundra vegetation. The palsas are typically characterized by lichens and evergreen dwarf shrubs (*Empetrum nigrum*, *Rhododendron tomentosum*, *Rubus chamaemorus*, *Vaccinium vitis-idaea*). The shallow ponds can feature a base moss layer (*Sphagnum spp.*), and fen areas are dominated by sedges and cottongrass (*Carex rotundata*, *Eriophorum scheuchzeri*, *Eriophorum rusciculatum*, *Eriophorum vaginatum*). The site features sporadic permafrost with organic-rich peat soils with a peat depth of around 155 cm (Kjellman et al., 2018) and active layer depths of up to 90 cm on the palsas.

We geo-referenced a historic aerial photograph taken in 1955 by the Norwegian Mapping Authority (Figure 1b, Kartverket survey WF-688 H-13) and conducted multiple drone surveys during our 3-year study period. We produced digital elevation models using the structure-from-motion technique (Ullman, 1979) from our drone imagery from 2019 to 2022, which we subtracted to estimate the surface subsidence. We classified the landscape at the site into three discrete surface types (palsas, ponds, fens) based on a visual inspection of our ortho-rectified drone imagery from 2019 (Figure 1a).

2.2. Eddy Covariance Flux Measurements

The EC flux system shown in Figure 2a was established at the I skoras site in March 2019. The data period in the present study covers 3 years, that is, until March 2022. The EC system consists of a CSAT3 three-dimensional sonic anemometer (Campbell Scientific, USA), an Li-7200 closed-path infrared gas analyzer for CO₂, as well as an Li-7700 open path gas analyzer for CH₄ (both Li-Cor, USA). The system is supplied with an off-grid power supply based on a wind generator and solar panels. An electronic relay is used to turn off the EC system when the battery voltage of the power supply becomes too low, while the sensors and logger of the ancillary measurements (described in Text S2 in Supporting Information S1), which consume only a fraction of the power of the EC system, continue to operate. We processed the EC raw data to 30 min flux estimates following the conventional EC methodology (Gu et al., 2012). After filtering the flux time series for unfavorable measurement conditions, for example, due to a lack of stationarity or turbulent mixing (see Text S1 in Supporting Information S1 for details), we are left with 11,334 and 4,743 valid half-hourly flux estimates for CO₂ and CH₄, respectively.

The total flux estimate from EC is the mathematical convolution of the surface flux distribution with the flux footprint function, which we estimate using the flux footprint model by Kljun et al. (2015). The resulting footprint weight-maps are combined with the surface type classification (see Section 2.1 and Figure 1a) to estimate the weight of the contribution of each of the three surface types (w_{palsa} , w_{ponds} , w_{fen}) to each 30-min EC flux estimate. The resulting average distribution (climatology) of these dynamic footprint weights is shown in Figure 1d.

2.3. Bayesian Neural Networks

For our BNN flux disaggregation model we use a fully connected feedforward neural network, also known as a multilayer perceptron, with 10 predictors as inputs (ancillary variables) and one total flux as output

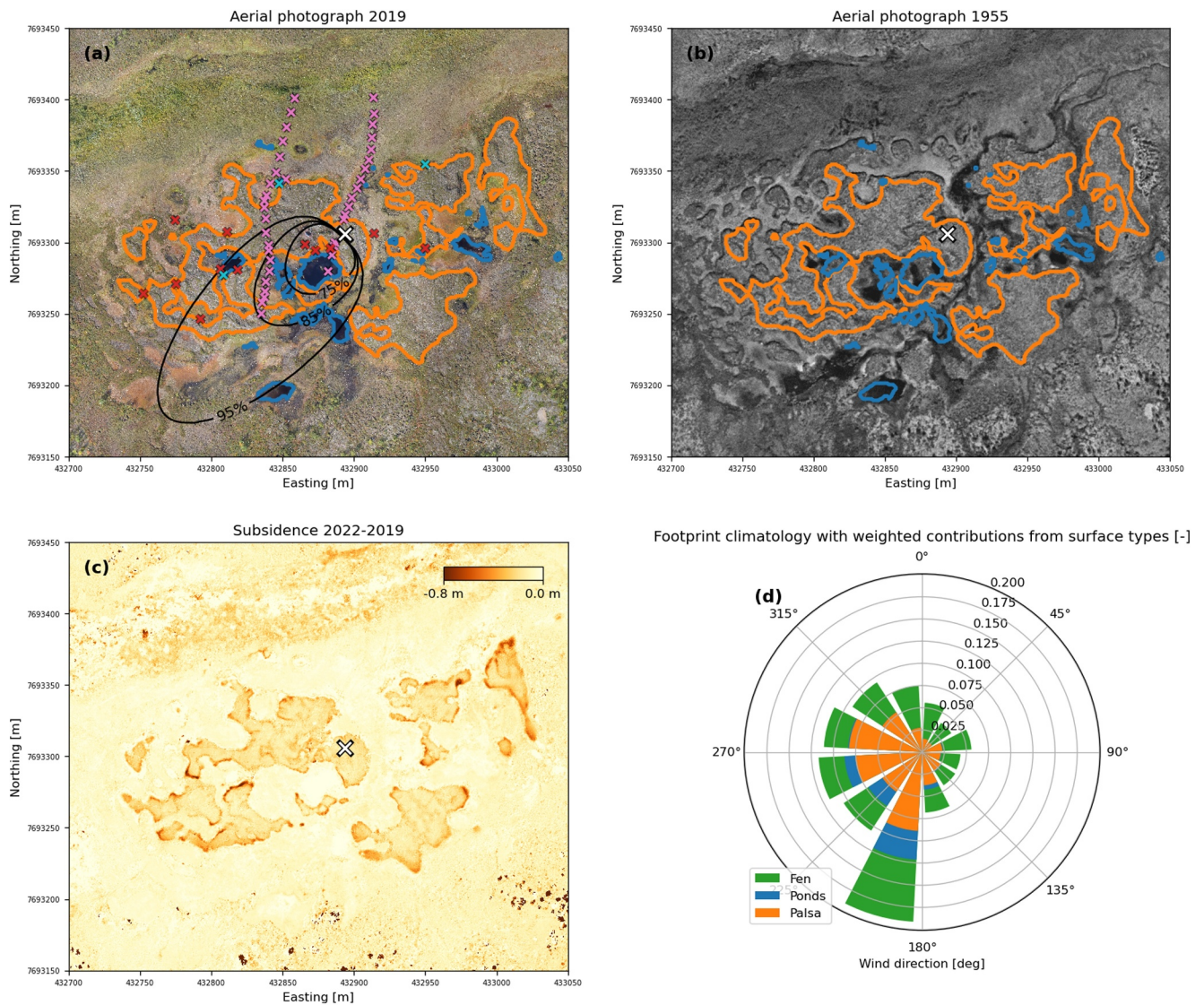


Figure 1. Surface characterization of the Iškoras permafrost peatland. (a) Ortho-rectified aerial photographs from 2019 with contour lines for palsa (orange) and pond (blue) areas (all other areas are classified as fen). The white cross marks the location of the flux tower, from which the black lines show an example of the 75%, 85%, and 95% contours of the cumulative flux footprint function for 25 July 2019, 16:00 UTC. Colored crosses indicate independent validation flux measurements by chambers (red), dissolved gas concentrations in ponds (cyan), and snowpack profiles (pink). (b) Ortho-rectified aerial photographs taken in 28 July 1955, overlain with the same contour lines for palsa and pond extent in 2019. (c) Vertical difference between elevation models from September 2022 and 2019 indicating surface subsidence. (d) Averaged footprint weights of all valid flux measurements plotted by the corresponding wind sectors. Colors indicate the footprint-weighted contribution of each surface type.

(either CO_2 or CH_4 , so we train two BNNs separately), as depicted in Figure 2b. We use a total of 300 nodes placed in five hidden layers with respectively 96, 48, 12, 48, and 96 nodes per layer, resembling the architecture of an auto-encoder (Goodfellow et al., 2016). This architecture results in a total of $N_p = 11,919$ parameters (network weights and biases) collectively denoted through the random vector $\theta \in \mathbb{R}^{N_p}$ that we infer. As is usually the case in deep learning there are thus more parameters than data points (Murphy, 2022), in which case the Bayesian approach adopted herein helps to regularize the problem and avoid overfitting (MacKay, 2003; Murphy, 2023). At each node, the inputs are multiplied by weights, summed, combined with an additive bias term, and passed through an activation function to produce the node's output. For all the hidden layers we employ the widely used Rectified Linear Unit (ReLU) non-linear activation function defined as $\text{ReLU}(x) = \max(0, x)$. Our BNN can be thought of as having two output layers with linear activation functions: the first output layer consists of three nodes, predicting the CO_2 or

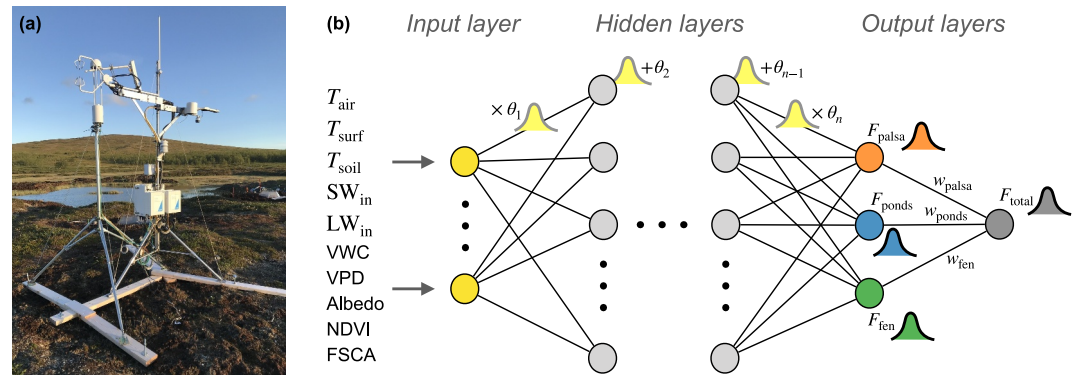


Figure 2. Flux estimation system. (a) The eddy covariance tower at the Iskoras permafrost peatland. (b) Conceptual architecture of our Bayesian neural network with uncertainty-aware parameters θ to estimate fluxes F of three different surface types and their weighted average with weights w_s based on the footprint model.

CH_4 fluxes for each of the three surface types based on the dynamic inputs $\mathbf{x}(t)$ and the (static) uncertain network parameters θ . In the second output layer, these fluxes are averaged using the deterministic dynamic footprint weights $w_s(t)$ for each surface type at the corresponding 30-min interval (see Section 2.2), predicting the total flux F_{total} that can be compared to observations from the EC system, that is,

$$F_{\text{total}}(\mathbf{w}_s, \mathbf{x}, \theta) = w_{\text{palsa}} F_{\text{palsa}}(\mathbf{x}, \theta) + w_{\text{ponds}} F_{\text{ponds}}(\mathbf{x}, \theta) + w_{\text{fen}} F_{\text{fen}}(\mathbf{x}, \theta) \quad (1)$$

This innovative network architecture with two consecutive output layers serves as the basis for the envisioned flux disaggregation between the three surface types. Note that this disaggregation assumes that the within-class flux is spatially homogeneous and can thus only estimate the spatial average of within-class flux dynamics.

The BNN parameters are initialized by drawing from a standard normal distribution as the (regularizing weakly informative) prior distribution (Banner et al., 2020). Unlike the more conventional approach of training a neural network by optimizing the parameters via backpropagation, we train our network parameters using (approximate) Bayesian inference techniques developed for geophysical data assimilation (Evensen et al., 2022), namely an iterative ensemble Kalman method (Emerick & Reynolds, 2013) (see details in Text S3 in Supporting Information S1). To better represent the typically multi-modal posterior parameter distributions (Izmailov et al., 2021), we repeat the BNN training 100 times with different random seeds to capture local modes and combine these 100 local ensembles to form a global ensemble, as a so-called deep ensembles approximation (Lakshminarayanan et al., 2017; Wilson & Izmailov, 2020) of the posterior predictive distribution (see Text S3 in Supporting Information S1). For the ensemble data assimilation-based BNN training, we assume a typical zero mean additive Gaussian observation error model with observation error standard deviations of $0.1 \mu\text{mol m}^{-2} \text{s}^{-1}$ for CO_2 and $2.5 \text{ nmol m}^{-2} \text{s}^{-1}$ for CH_4 . As predictors, we use air, surface, and soil temperature (T_{air} , T_{surf} , and T_{soil} , respectively), vapor pressure deficit (VPD), shortwave and longwave incoming radiation (SW_{in} and LW_{in} , respectively), albedo, fractional snow-covered area (FSCA), the Normalized Difference Vegetation index (NDVI), and soil volumetric water content (VWC), estimated from in-situ measurements and remote sensing data as described in Text S2 in Supporting Information S1. Figure S2 in Supporting Information S1 shows the scatter plot matrix of the predictors, fluxes, and footprint weights, which are all archived and available (Pirk, 2023). As the predictors are available continuously for the entire 3 year campaign, the BNN can simultaneously perform both flux disaggregation and gap-filling.

A performance evaluation for the prediction of the total flux using a common 80%–20% train-test split (Murphy, 2022) indicates good prediction accuracy and generalization, with normalized root mean square error values of between 5% and 11% for both train and test data sets (Figure S4 in Supporting Information S1). The coefficients of determination (R^2) for CO_2 range between 0.7 and 0.8. For CH_4 , we notice that while the dynamics of daily average fluxes are well captured in the BNN model ($0.71 < R^2 < 0.72$), the model performs notably worse for the dynamics of the instantaneous 30-min fluxes ($0.28 < R^2 < 0.29$), see discussion in Section 3.3.

2.4. Independent Flux Validation

As an independent validation of the disaggregated flux results, we conducted manual measurement campaigns to estimate fluxes on the plot scale using flux chambers, dissolved gas concentrations, and snowpack gradients. The sampling locations were distributed around the EC tower as shown in Figure 1a. Chamber flux measurements of CO₂ and CH₄ were performed in palsa and fen areas on 2–3 July 2021, and 11 September 2021. We used a Li-7810 gas analyzer (Li-Cor, USA), with a plexiglass chamber covering 25 × 25 cm², and followed Pedersen et al. (2010) to estimate fluxes from the measured concentration sequences. Dissolved concentrations of CO₂ and CH₄ were measured in the surface waters in three ponds (not including the largest pond) with the acidified headspace technique (Valiente et al., 2022) at five occasions during the snow-free season, ranging between 40 and 520 μmol L⁻¹ for CO₂, and between 1.1 and 26 μmol L⁻¹ for CH₄. Pond fluxes were estimated from these dissolved gas concentrations following the methodology in Clayer et al. (2021), using the surface renewal gas exchange model by MacIntyre et al. (2010) for the gas transfer velocity, accounting for the small pond sizes (Vachon & Prairie, 2013) and the typically low wind speeds at Iškoras (Crusius & Wanninkhof, 2003). We conducted a survey of snowpack CH₄ concentrations on 14 March 2023, to estimate the magnitude and direction of wintertime CH₄ fluxes for all three surface types. Here, we used a portable CH₄ laser spectrometer (MIRA Strato, Aeris Technologies, USA) and estimated diffusive CH₄ emission from snowpack concentration gradients using the methodology described in Pirk et al. (2016) (see Figure S5 in Supporting Information S1 for examples of concentration time series as well as snowpack density and temperature profiles).

3. Results and Discussion

3.1. Disaggregated Fluxes of Palsas, Ponds, and Fens

The estimated mean flux dynamics shown in Figures 3a–3f indicate a clear separation of fluxes from the three surface types achieved by our BNN model. All surface types show a seasonal cycle of CO₂ and CH₄ flux dynamics. In summertime, after snow melt-out, CO₂ fluxes exhibit diurnal cycles as expected for northern latitude ecosystems. For CH₄, there is a relatively weak indication of such diurnal cycles for pond and fen surfaces, possibly due to the diurnal cycle of the ground temperature regulating CH₄ production rates.

The (posterior ensemble mean) CO₂ flux of dry palsa areas ranges from -2.4 to 1.4 μmol m⁻² s⁻¹ during the 3 year study period. Palsa CH₄ fluxes are relatively insignificant, but show persistent negative values with a (posterior median) temporal average of -1.8 (-4.8, 1.2) nmol m⁻² s⁻¹, where the credible interval in brackets shows the posterior 25th and 75th percentile. This CH₄ uptake is consistent with our validation chambers measurements in summertime with estimates of -1.2 (-1.8, -0.5) nmol m⁻² s⁻¹ and snowpack gas gradients in wintertime with estimates of -0.04 (-0.09, 0.01) nmol m⁻² s⁻¹ as shown in Figure S6 in Supporting Information S1.

Thermokarst ponds are estimated to emit CO₂ at rates of up to 5.0 μmol m⁻² s⁻¹, which is relatively high compared to flux estimates from thermokarst ponds in permafrost peatlands in Canada (around 2.8 μmol m⁻² s⁻¹ (Matveev et al., 2016)) and Sweden (average of 3.2 μmol m⁻² s⁻¹ (Kuhn et al., 2018)) that are based on measurements that typically exclude ebullition. The magnitude and seasonal pattern of our BNN emission estimates are in very good agreement with our independent flux estimates from the dissolved gas measurements (Figure S6 in Supporting Information S1). The observed diurnal cycle of the summertime CO₂ emission from the ponds could be due to periodic overturning of the water column or photo dissociation of dissolved organic carbon in the surface water. Parts of this carbon can originate from collapsing palsa edges releasing labile organic carbon (Patzner et al., 2022), as documented for our site in Figure 1c. Pond CH₄ fluxes reach up to 73 nmol m⁻² s⁻¹, which is on the lower end of the range supported by our dissolved gas measurements, which may be attributed to differences between ponds as no water samples could be taken from the largest pond that dominates the pond flux signal in our EC measurements. The relative seasonal CH₄ flux patterns still agree well, also with the wintertime average snowpack flux estimates of 1.4 (0.1, 1.6) nmol m⁻² s⁻¹ as shown in Figure S6 in Supporting Information S1. For reference, Matveev et al. (2016) report maximum diffusive CH₄ emissions from the aforementioned Canadian thermokarst ponds of around 120 nmol m⁻² s⁻¹, which is notably higher than our maximum pond CH₄ flux.

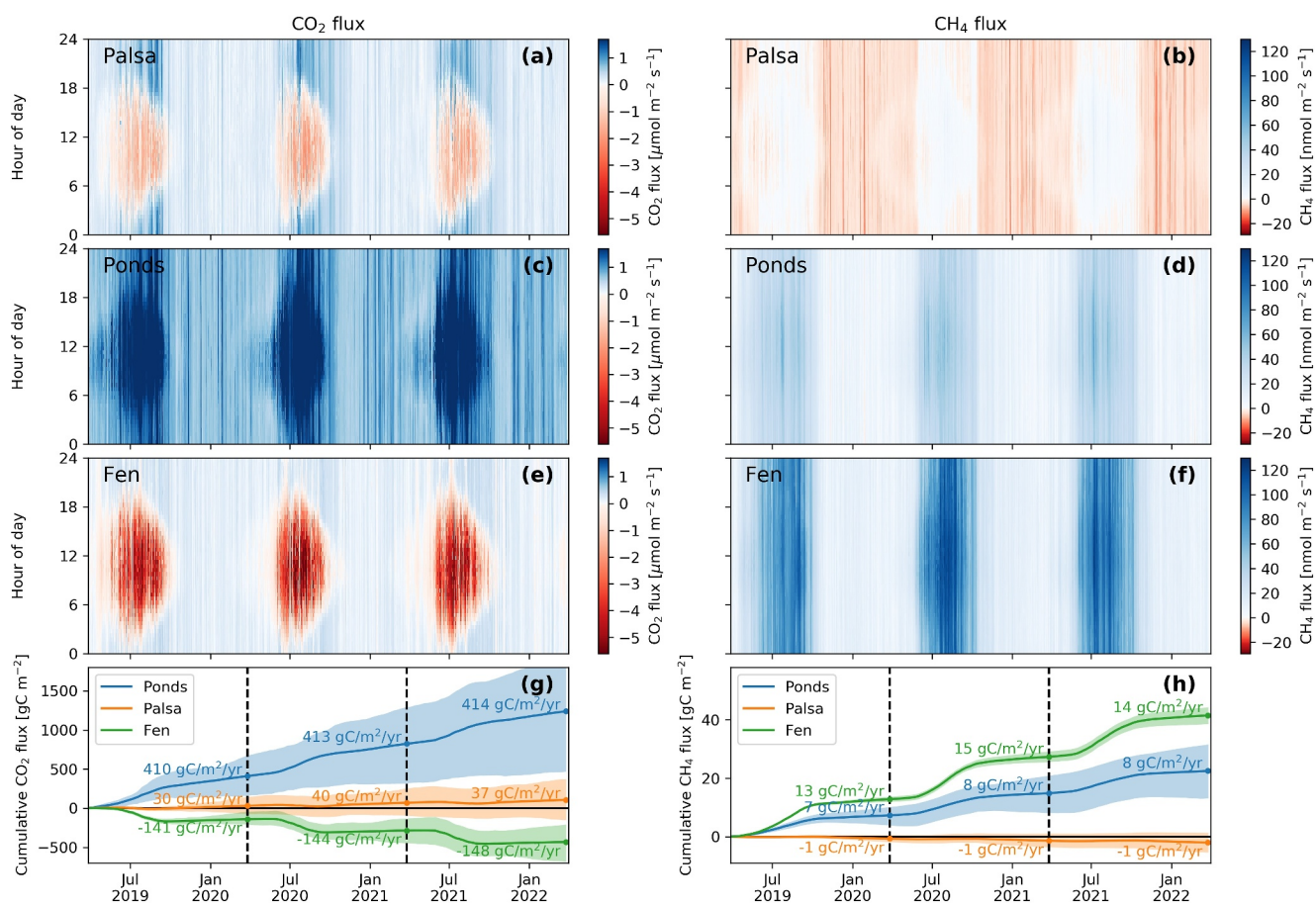


Figure 3. Flux dynamics and budgets. (a–f): Posterior mean CO₂ (left) and CH₄ (right) flux predictions for the three surface types as fingerprint plots using the same color scale. (g–h): Corresponding cumulative CO₂ and CH₄ fluxes with uncertainty bands representing the posterior ensemble’s interquartile range. Stipulated vertical lines indicate 1-year intervals for which the numbers indicate annual budgets.

Among the three surface classes, fens feature the largest maximum CO₂ uptake ($7.0 \mu\text{mol m}^{-2} \text{s}^{-1}$, i.e., three times higher uptake flux than the palsas) and the largest maximum CH₄ release ($134 \text{ nmol m}^{-2} \text{s}^{-1}$, i.e., almost two times higher release flux than the ponds). The estimated CO₂ fluxes are consistent with our chamber fluxes in summertime (Figure S6 in Supporting Information S1), and the large estimated CH₄ fluxes are also corroborated by summertime chamber fluxes (average of $133 (86, 171) \text{ nmol m}^{-2} \text{s}^{-1}$) and snowpack fluxes in wintertime (average of $8.0 (4.5, 9.7) \text{ nmol m}^{-2} \text{s}^{-1}$).

The annual budgets of all these fluxes are relatively similar across the 3 years of our measurement campaign which featured no outliers in the climatic conditions, which is in line with findings from other multi-year flux studies in the sub-Arctic (e.g., Christensen et al., 2012). The cumulative carbon balance of each surface type is dominated by CO₂ fluxes (Figures 3g and 3h). Palsa surfaces are moderate carbon sources ($35 \text{ gC m}^{-2} \text{yr}^{-1}$ on average), while fen areas feature a strong carbon sink ($-131 \text{ gC m}^{-2} \text{yr}^{-1}$ on average, after accounting for CH₄ release). Ponds, while only a small area in the EC footprint and therefore most uncertain, are strong carbon emission hotspots, releasing on average $420 \text{ gC m}^{-2} \text{yr}^{-1}$ to the atmosphere as CO₂ and CH₄ combined. For CH₄, the relative difference between surface types is larger than for CO₂, with fens emitting most (on average $14 \text{ gC m}^{-2} \text{yr}^{-1}$), followed by ponds ($7.5 \text{ gC m}^{-2} \text{yr}^{-1}$), and a small CH₄ sink in palsa areas ($-0.7 \text{ gC m}^{-2} \text{yr}^{-1}$). These CH₄ annual budgets are in general similar to those reported in a arctic-boreal synthesis compiled by Kuhn et al. (2021), which reports CH₄ emissions with an interquartile range between 4.5 and $29 \text{ gC m}^{-2} \text{yr}^{-1}$ for fens, 3.3 and $52 \text{ gC m}^{-2} \text{yr}^{-1}$ for diffusion and ebullition from small peatland ponds, and -0.3 to $0.5 \text{ gC m}^{-2} \text{yr}^{-1}$ for dry tundra.

3.2. Climate Feedbacks and Geomorphological Trajectory

Thermokarst ponds and lakes are currently estimated to cover about 7% of the permafrost region, and wetland thermokarst landscapes (including fens) cover a similar proportion of about 8% (Olefeldt et al., 2016). However, most areas of Fennoscandia and Western Siberia are projected to become climatically unsuitable to sustain permafrost peatlands over the next century, suggesting transformations in the landscapes that can leave an estimated 39 Gt of permafrost carbon (equivalent to twice the amount of carbon stored in European forests) vulnerable to post-thaw decomposition (Fewster et al., 2022; Hugelius et al., 2020). Our CO₂ and CH₄ flux budgets allow for a direct assessment of the fate of these carbon stocks in permafrost peatlands, and their effect on the atmospheric energy budget through greenhouse gas forcing. To this end, we combine the mean annual CO₂ and CH₄ budgets of each surface type to CO₂-equivalent fluxes using a 100-year global warming potential for CH₄ of 27 (Forster et al., 2021). Thus, the 3-year mean (credible interval) CO₂-equivalent flux is estimated to be 106 gCO₂ m⁻² yr⁻¹ (−252 to 469 gCO₂ m⁻² yr⁻¹) for palsas, 1,780 gCO₂ m⁻² yr⁻¹ (725–2,834 gCO₂ m⁻² yr⁻¹) for ponds, and −31 gCO₂ m⁻² yr⁻¹ (−375 to 274 gCO₂ m⁻² yr⁻¹) for fens. The present day areal fraction of surface types contributing to the EC signal (52% palsa, 7% ponds, and 41% fen according to our EC footprint climatology shown in Figure 1d) suggests that the Iškoras site is currently a source of atmospheric carbon with a CO₂-equivalent flux of 167 gCO₂ m⁻² yr⁻¹. Using a space-for-time substitution, the ratios of the CO₂-equivalent fluxes indicate that palsa degradation to thermokarst ponds would lead to a 17 fold increase in the local greenhouse gas forcing, while palsa transformation into fens would reduce the local greenhouse gas forcing to slightly negative values.

Simulations by Aas et al. (2019) indicate that the degradation of permafrost peatlands in northern Norway is likely to accelerate in the next three to four decades. If and when palsa degradation creates ponds or fens will depend on the degradation rate and the amount of excess ice at the site (fast collapse at ice-rich sites likely favors pond formation). The geophysical interplay of processes causing lake formation and subsequent terrestrialization through drainage and infilling with fen vegetation is, however, still hard to predict. This complexity is exemplified by Nitze et al. (2018) who report both increasing and decreasing trends in limnidity (i.e., the areal fraction of ponds and lakes) for different parts of the permafrost region. Moreover, even an overall constant limnidity in a region can mask extensive lake drainage combined with new thermokarst lake formation (Sannel & Kuhry, 2011). Future studies combining even more Earth observations could help to refine our understanding of permafrost peatlands and upscale our benchmark of the greenhouse gas exchange beyond our EC footprint.

3.3. Bayesian Deep Learning for Flux Disaggregation

Using the BNN model for flux gap-filling and disaggregation yields considerable flexibility, generalization, and predictive accuracy, but comes at the cost of limited interpretability (Rudin, 2019), as the parameters of this black box model are not directly associated with any real-world process. At the same time, to the best of our knowledge, no interpretable mechanistic modeling approaches exist for EC flux disaggregation. In the interim, the BNN proposed herein serves as an uncertainty- and sparsity-aware data-driven approach that can help guide future method developments. For example, the relatively large posterior predictive uncertainty in pond fluxes and annual budgets emerges naturally in our BNN model as a consequence of the limited information content in the measurements (because ponds only cover about 7% of the EC footprint) and the difficulty to describe important processes like ebullition with the available predictors. Ponds are now identified as the key remaining uncertainty in this landscape, so that future studies can target this landscape element more specifically. The flux disaggregation approach can also be used to validate emerging drone data assimilation-based flux estimation methods (Pirk et al., 2022), guide land surface model developments (Aas et al., 2019), and incorporate uncertainty in flux gap filling approaches (Pirk et al., 2023).

Neural networks are in principle universal function approximators (Hornik et al., 1989), but we must assume that unobserved fluxes follow the same predictor relationship as the observed fluxes. The good generalization seen in our train-test split evaluation (Figure S4 in Supporting Information S1) suggests that our CO₂ and CH₄ flux data sets are sufficiently representative. Interestingly, our BNN model for CH₄ flux has a low value of R^2 (around 0.3) for instantaneous CH₄ fluxes compared to daily average fluxes (R^2 around 0.7), which could be related to “unpredictable” ebullition events, or, more generally, to important but unobserved predictor variables. Compared to CO₂, CH₄ dynamics likely have a stronger dependency on processes occurring in the soil (Treat et al., 2015), where conditions change on small spatial scales and only few sensors were available, so that many of the control

mechanisms are only indirectly captured through our surface and atmospheric sensors. A spatially distributed network of soil sensors could be employed to reduce the associated uncertainty.

Despite the partly opposing flux directions (release vs. uptake) between the three surface types, the BNN flux disaggregation yields realistic flux magnitudes without clear indications of equifinality problems (e.g., large fluxes in opposing directions). Future work could explore other network architectures for flux data analysis, such as recurrent or convolutional networks, combined with marginal likelihood methods for hyperparameter and architecture optimization (Murphy, 2023). Another aspect with potential for improvement is the assumption of deterministic footprint weights w_s between the ultimate layers of the BNN. Here, future studies could use an ensemble of footprint models representing the uncertainty in the footprint input parameters using uncertain hyperparameters that are then inferred from the measurements together with the other network parameters. Such approaches could result in even better calibration of flux uncertainties.

4. Conclusions

Representative, high resolution, and uncertainty-aware flux estimates are invaluable to confidently assess land-atmosphere interactions in heterogeneous and dynamic ecosystems like permafrost peatlands. To achieve this goal, we developed an ensemble-based BNN model for EC flux disaggregation, which we compared against three other flux estimation methods. These independent flux estimates are compatible with our BNN results, but their large spatial variability also demonstrate the challenges to obtain landscape-scale flux measurements with manual sampling techniques.

Our BNN results indicate that while tundra areas have a near-zero annual CH_4 balance, the fens and ponds that form upon tundra degradation emit large amounts of CH_4 . Fens compensate this greenhouse gas forcing with a strong annual CO_2 sink, while ponds are also strong—yet uncertain— CO_2 emission hotspots. Our flux results indicate that tundra degradation to thermokarst ponds would lead to a 17 fold increase in the local greenhouse gas forcing, while transformation into fens would reduce the local greenhouse gas forcing.

Data Availability Statement

Processed flux and ancillary data are available in Pirk (2023). The code for flux inference is available in Pirk and Aalstad (2023).

References

- Aas, K. S., Martin, L., Nitzbon, J., Langer, M., Boike, J., Lee, H., et al. (2019). Thaw processes in ice-rich permafrost landscapes represented with laterally coupled tiles in a land surface model. *The Cryosphere*, 13(2), 591–609. <https://doi.org/10.5194/tc-13-591-2019>
- Baldocchi, D. D. (2020). How eddy covariance flux measurements have contributed to our understanding of *Global Change Biology*. *Global Change Biology*, 26(1), 242–260. <https://doi.org/10.1111/gcb.14807>
- Banner, K. M., Irvine, K. M., & Rodhouse, T. J. (2020). The use of Bayesian priors in Ecology: The good, the bad and the not great. *Methods in Ecology and Evolution*, 11(8), 882–889. <https://doi.org/10.1111/2041-210X.13407>
- Borge, A. F., Westermann, S., Solheim, I., & Etzelmüller, B. (2017). Strong degradation of palsas and peat plateaus in northern Norway during the last 60 years. *The Cryosphere*, 11(1), 1–16. <https://doi.org/10.5194/tc-11-1-2017>
- Burke, S. A., Wik, M., Lang, A., Contosta, A. R., Palace, M., Crill, P. M., & Varner, R. K. (2019). Long-term measurements of methane ebullition from thaw ponds. *Journal of Geophysical Research: Biogeosciences*, 124(7), 2208–2221. <https://doi.org/10.1029/2018JG004786>
- Christensen, T. R., Jackowicz-Korczyński, M., Aurela, M., Crill, P., Heliasz, M., Mastepanov, M., & Friborg, T. (2012). Monitoring the multi-year carbon balance of a subarctic tundra mire with micrometeorological techniques. *Ambio*, 41(S3), 207–217. <https://doi.org/10.1007/s13280-012-0302-5>
- Clare, M. C. A., Sonnewald, M., Lguensat, R., Deshayes, J., & Balaji, V. (2022). Explainable artificial intelligence for Bayesian neural networks: Toward trustworthy predictions of ocean dynamics. *Journal of Advances in Modeling Earth Systems*, 14(11), e2022MS003162. <https://doi.org/10.1029/2022MS003162>
- Clayer, F., Thrane, J.-E., Brandt, U., Dörsch, P., & Wit, H. A. (2021). Boreal headwater catchment as hot spot of carbon processing from headwater to fjord. *Journal of Geophysical Research: Biogeosciences*, 126(12), e2021JG006359. <https://doi.org/10.1029/2021JG006359>
- Crusius, J., & Wanninkhof, R. (2003). Gas transfer velocities measured at low wind speed over a lake. *Limnology & Oceanography*, 48(3), 1010–1017. <https://doi.org/10.4319/lo.2003.48.3.1010>
- Emerick, A. A., & Reynolds, A. C. (2013). Ensemble smoother with multiple data assimilation. *Computers & Geosciences*, 55, 3–15. <https://doi.org/10.1016/j.cageo.2012.03.011>
- Evensen, G., Vossepoel, F. C., & van Leeuwen, P. J. (2022). *Data assimilation fundamentals: A unified formulation of the state and parameter estimation problem*. Springer. <https://doi.org/10.1007/978-3-030-96709-3>
- Fewster, R. E., Morris, P. J., Ivanovic, R. F., Swindles, G. T., Peregon, A. M., & Smith, C. J. (2022). Imminent loss of climate space for permafrost peatlands in Europe and Western Siberia. *Nature Climate Change*, 12(4), 373–379. <https://doi.org/10.1038/s41558-022-01296-7>
- Forster, P., Storelvmo, T., Armour, K., Collins, W., Dufresne, J.-L., Frame, D., et al. (2021). Chapter 7: The Earth's energy budget, climate feedbacks, and climate sensitivity. <https://doi.org/10.25455/wgtn.16869671.v1>

Acknowledgments

We would like to thank our engineers John Hulth, Luc Girod, and Trond Eiken for their help with field measurements and drone imagery processing, as well as Jacqueline Knutson for water sample collection. The work was supported by the Research Council of Norway (projects #301552, #294948, #160016, and #323945) and the European Research Council (project #101116083). This work is a contribution to the strategic research initiative LATICE (#Uio/GEO103920), the Center for Biogeochemistry in the Anthropocene, as well as the Center for Computational and Data Science at the University of Oslo. The study contains modified Copernicus Sentinel data [Year 2019, 2020, 2021, 2022] obtained from the Google Earth Engine.

- Frei, E. R., Schnell, L., Vitasse, Y., Wohlgemuth, T., & Moser, B. (2020). Assessing the effectiveness of in-situ active warming combined with open top chambers to study plant responses to climate change. *Frontiers in Plant Science*, *11*. <https://doi.org/10.3389/fpls.2020.539584>
- Ghahramani, Z. (2015). Probabilistic machine learning and artificial intelligence. *Nature*, *521*(7553), 452–459. <https://doi.org/10.1038/nature14541>
- Goodfellow, I., Bengio, Y., & Courville, A. (2016). *Deep learning*. MIT Press.
- Griebel, A., Bennett, L. T., Metzen, D., Cleverly, J., Burba, G., & Arndt, S. K. (2016). Effects of inhomogeneities within the flux footprint on the interpretation of seasonal, annual, and interannual ecosystem carbon exchange. *Agricultural and Forest Meteorology*, *221*, 50–60. <https://doi.org/10.1016/j.agrformet.2016.02.002>
- Grosse, G., Jones, B., & Arp, C. (2013). 8.21 thermokarst lakes, drainage, and drained basins. In *Treatise on geomorphology* (pp. 325–353). Elsevier. <https://doi.org/10.1016/B978-0-12-374739-6.00216-5>
- Gu, L., Massman, W. J., Leuning, R., Pallardy, S. G., Meyers, T., Hanson, P. J., et al. (2012). The fundamental equation of eddy covariance and its application in flux measurements. *Agricultural and Forest Meteorology*, *152*, 135–148. <https://doi.org/10.1016/j.agrformet.2011.09.014>
- Holmes, M. E., Crill, P. M., Burnett, W. C., McCalley, C. K., Wilson, R. M., Frolking, S., et al. (2022). Carbon accumulation, flux, and fate in Stordalen Mire, a permafrost peatland in transition. *Global Biogeochemical Cycles*, *36*(1). <https://doi.org/10.1029/2021GB007113>
- Hornik, K., Stinchcombe, M., & White, H. (1989). Multilayer feedforward networks are universal approximators. *Neural Networks*, *2*(5), 359–366. [https://doi.org/10.1016/0893-6080\(89\)90020-8](https://doi.org/10.1016/0893-6080(89)90020-8)
- Hugelius, G., Loisel, J., Chadburn, S., Jackson, R. B., Jones, M., MacDonald, G., et al. (2020). Large stocks of peatland carbon and nitrogen are vulnerable to permafrost thaw. *Proceedings of the National Academy of Sciences of the United States of America*, *117*(34), 20438–20446. <https://doi.org/10.1073/pnas.1916387117>
- Izmailov, P., Vikram, S., Hoffman, M. D., & Wilson, A. G. G. (2021). What are Bayesian neural network posteriors really like? In M. Meila & T. Zhang (Eds.), *Proceedings of the 38th international conference on machine learning* (Vol. 139, pp. 4629–4640). PMLR.
- Jiao, Y., Davie-Martin, C. L., Kramshøj, M., Christiansen, C. T., Lee, H., Althuizen, I. H., & Rinnan, R. (2023). Volatile organic compound release across a permafrost-affected peatland. *Geoderma*, *430*, 116355. <https://doi.org/10.1016/j.geoderma.2023.116355>
- Kjellman, S. E., Axelsson, P. E., Ertelz Müller, B., Westermann, S., & Sannel, A. B. K. (2018). Holocene development of subarctic permafrost peatlands in Finnmark, northern Norway. *The Holocene*, *28*(12), 1855–1869. <https://doi.org/10.1177/0959683618798126>
- Kljun, N., Calanca, P., Rotach, M. W., & Schmid, H. P. (2015). A simple two-dimensional parameterisation for Flux Footprint Prediction (FFP). *Geoscientific Model Development*, *8*(11), 3695–3713. <https://doi.org/10.5194/gmd-8-3695-2015>
- Krizhevsky, A., Sutskever, I., & Hinton, G. E. (2012). Imagenet classification with deep convolutional neural networks. In F. Pereira, C. Burges, L. Bottou, & K. Weinberger (Eds.), *Advances in neural information processing systems* (Vol. 25).
- Kuhn, M., Lundin, E. J., Giesler, R., Johansson, M., & Karlsson, J. (2018). Emissions from thaw ponds largely offset the carbon sink of northern permafrost wetlands. *Scientific Reports*, *8*(1), 9535. <https://doi.org/10.1038/s41598-018-27770-x>
- Kuhn, M. A., Varner, R. K., Bastviken, D., Crill, P., MacIntyre, S., Turetsky, M., et al. (2021). Bawld- CH_4 : A comprehensive dataset of methane fluxes from boreal and arctic ecosystems. *Earth System Science Data*, *13*(11), 5151–5189. <https://doi.org/10.5194/essd-13-5151-2021>
- Kutzbach, L., Schneider, J., Sachs, T., Giebels, M., Nykänen, H., Shurpali, N. J., et al. (2007). CO_2 flux determination by closed-chamber methods can be seriously biased by inappropriate application of linear regression. *Biogeosciences*, *4*(6), 1005–1025. <https://doi.org/10.5194/bg-4-1005-2007>
- Lakshminarayanan, B., Pritzel, A., & Blundell, C. (2017). Simple and scalable predictive uncertainty estimation using deep ensembles. In I. Guyon, U. Von Luxburg, S. Bengio, H. Wallach, R. Fergus, S. Vishwanathan, & R. Garnett (Eds.), *Advances in neural information processing systems* (Vol. 30). Curran Associates, Inc.
- Lawrence, D. M., Fisher, R. A., Koven, C. D., Oleson, K. W., Swenson, S. C., Bonan, G., et al. (2019). The Community Land Model Version 5: Description of new features, benchmarking, and impact of forcing uncertainty. *Journal of Advances in Modeling Earth Systems*, *11*(12), 4245–4287. <https://doi.org/10.1029/2018MS001583>
- LeCun, Y., Bengio, Y., & Hinton, G. (2015). Deep learning. *Nature*, *521*(7553), 436–444. <https://doi.org/10.1038/nature14539>
- Levy, P., Drewer, J., Jammot, M., Leeson, S., Friberg, T., Skiba, U., & van Oijen, M. (2020). Inference of spatial heterogeneity in surface fluxes from eddy covariance data: A case study from a subarctic mire ecosystem. *Agricultural and Forest Meteorology*, *280*, 107783. <https://doi.org/10.1016/j.agrformet.2019.107783>
- Lopez-Gomez, I., Christopoulos, C., Langeland Ervik, H. L., Dunbar, O. R. A., Cohen, Y., & Schneider, T. (2022). Training physics-based machine-learning parameterizations with gradient-free ensemble Kalman methods. *Journal of Advances in Modeling Earth Systems*, *14*(8), e2022MS003105. <https://doi.org/10.1029/2022MS003105>
- Luoto, M., & Seppälä, M. (2003). Thermokarst ponds as indicators of the former distribution of palsas in Finnish Lapland: Thermokarst Development from Palsas. *Permafrost and Periglacial Processes*, *14*(1), 19–27. <https://doi.org/10.1002/ppp.441>
- MacIntyre, S., Jonsson, A., Jansson, M., Aberg, J., Turney, D. E., & Miller, S. D. (2010). Buoyancy flux, turbulence, and the gas transfer coefficient in a stratified lake. *Geophysical Research Letters*, *37*(24), L24604. <https://doi.org/10.1029/2010GL044164>
- MacKay, D. J. C. (2003). *Information theory, inference, and learning algorithms*. Cambridge University Press.
- Martin, L. C. P., Nitzbon, J., Scheer, J., Aas, K. S., Eiken, T., Langer, M., et al. (2021). Lateral thermokarst patterns in permafrost peat plateaus in northern Norway. *The Cryosphere*, *15*(7), 3423–3442. <https://doi.org/10.5194/tc-15-3423-2021>
- Matveev, A., Laurion, I., Deshpande, B. N., Bhiry, N., & Vincent, W. F. (2016). High methane emissions from thermokarst lakes in subarctic peatlands: Methane Emissions from Peatland thermokarst lakes. *Limnology & Oceanography*, *61*(S1), S150–S164. <https://doi.org/10.1002/lno.10311>
- Murphy, K. P. (2022). *Probabilistic machine learning: An introduction*. MIT Press.
- Murphy, K. P. (2023). *Probabilistic machine learning: Advanced topics*. MIT Press.
- Neal, R. M. (1996). *Bayesian learning for neural networks*. Springer. <https://doi.org/10.1007/978-1-4612-0745-0>
- Nitze, I., Grosse, G., Jones, B. M., Romanovsky, V. E., & Boike, J. (2018). Remote sensing quantifies widespread abundance of permafrost region disturbances across the Arctic and Subarctic. *Nature Communications*, *9*(1), 5423. <https://doi.org/10.1038/s41467-018-07663-3>
- Nykanen, H., Heikkinen, J. E. P., Pirinen, L., Tiilikainen, K., & Martikainen, P. J. (2003). Annual CO_2 exchange and CH_4 fluxes on a subarctic palsa mire during climatically different years. *Global Biogeochemical Cycles*, *17*(1), 1018. <https://doi.org/10.1029/2002GB001861>
- Oechel, W. C., Vourlitis, G. L., Hastings, S. J., Zulueta, R. C., Hinzman, L., & Kane, D. (2000). Acclimation of ecosystem CO_2 exchange in the Alaskan Arctic in response to decadal climate warming. *Nature*, *406*(6799), 978–981. <https://doi.org/10.1038/35023137>
- Olchev, A., Zyrianov, V., Panov, A., Sotosina, E., Mukhartova, I., Novenko, E., & Prokushkin, A. (2022). Seasonal variability of carbon dioxide and methane fluxes in a subarctic palsa mire in North-Central Siberia. In *ECAS 2022* (p. 52). <https://doi.org/10.3390/ecas2022-12837>
- Olefeldt, D., Goswami, S., Grosse, G., Hayes, D., Hugelius, G., Kuhry, P., et al. (2016). Circumpolar distribution and carbon storage of thermokarst landscapes. *Nature Communications*, *7*(1), 13043. <https://doi.org/10.1038/ncomms13043>

- Patzner, M. S., Logan, M., McKenna, A. M., Young, R. B., Zhou, Z., Joss, H., et al. (2022). Microbial iron cycling during palsa hillslope collapse promotes greenhouse gas emissions before complete permafrost thaw. *Communications Earth & Environment*, 3(1), 76. <https://doi.org/10.1038/s43247-022-00407-8>
- Pedersen, A. R., Petersen, S. O., & Schelde, K. (2010). A comprehensive approach to soil-atmosphere trace-gas flux estimation with static chambers. *European Journal of Soil Science*, 61(6), 888–902. <https://doi.org/10.1111/j.1365-2389.2010.01291.x>
- Pirk, N. (2023). Resources for “disaggregating the carbon exchange of degrading permafrost peatlands using Bayesian deep learning” [Dataset]. Zenodo. <https://doi.org/10.5281/zenodo.7913027>
- Pirk, N., & Aalstad, K. (2023). Deep ensemble flux inference [Software]. *GitHub*. Retrieved from https://github.com/norberp/deep_ensemble_flux_inference
- Pirk, N., Aalstad, K., Westermann, S., Vatne, A., van Hove, A., Tallaksen, L. M., et al. (2022). Inferring surface energy fluxes using drone data assimilation in large eddy simulations. *Atmospheric Measurement Techniques*, 15(24), 7293–7314. <https://doi.org/10.5194/amt-15-7293-2022>
- Pirk, N., Aalstad, K., Yilmaz, Y. A., Vatne, A., Popp, A. L., Horvath, P., et al. (2023). Snow–vegetation–atmosphere interactions in alpine tundra. *Biogeosciences*, 20(11), 2031–2047. <https://doi.org/10.5194/bg-20-2031-2023>
- Pirk, N., Tamstorf, M. P., Lund, M., Mastepanov, M., Pedersen, S. H., Mylius, M. R., et al. (2016). Snowpack fluxes of methane and carbon dioxide from high Arctic tundra. *Journal of Geophysical Research: Biogeosciences*, 121(11), 2886–2900. <https://doi.org/10.1002/2016JG003486>
- Qiu, C., Zhu, D., Ciais, P., Guenet, B., Krinner, G., Peng, S., et al. (2018). ORCHIDEE-PEAT (revision 4596), a model for northern peatland CO₂, water, and energy fluxes on daily to annual scales. *Geoscientific Model Development*, 11(2), 497–519. <https://doi.org/10.5194/gmd-11-497-2018>
- Reichstein, M., Camps-Valls, G., Stevens, B., Jung, M., Denzler, J., Carvalhais, N., & Prabhat, F. (2019). Deep learning and process understanding for data-driven Earth system science. *Nature*, 566(7743), 195–204. <https://doi.org/10.1038/s41586-019-0912-1>
- Rudin, C. (2019). Stop explaining black box machine learning models for high stakes decisions and use interpretable models instead. *Nature Machine Intelligence*, 1(5), 206–215. <https://doi.org/10.1038/s42256-019-0048-x>
- Sannel, A. B. K., & Kuhry, P. (2011). Warming-induced destabilization of peat plateau/thermokarst lake complexes. *Journal of Geophysical Research*, 116(G3), G03035. <https://doi.org/10.1029/2010JG001635>
- Schuur, E. A. G., McGuire, A. D., Schädel, C., Grosse, G., Harden, J. W., Hayes, D. J., et al. (2015). Climate change and the permafrost carbon feedback. *Nature*, 520(7546), 171–179. <https://doi.org/10.1038/nature14338>
- Serikova, S., Pokrovsky, O. S., Laudon, H., Krickov, I. V., Lim, A. G., Manasypov, R. M., & Karlsson, J. (2019). High carbon emissions from thermokarst lakes of Western Siberia. *Nature Communications*, 10(1), 1552. <https://doi.org/10.1038/s41467-019-09592-1>
- Treat, C. C., Natali, S. M., Ernakovich, J., Iversen, C. M., Lupascu, M., McGuire, A. D., et al. (2015). A pan-arctic synthesis of ch₄ and co₂ production from anoxic soil incubations. *Global Change Biology*, 21(7), 2787–2803. <https://doi.org/10.1111/gcb.12875>
- Ullman, S. (1979). The interpretation of structure from motion. *Proceedings of the Royal Society of London. Series B. Biological Sciences*, 203(1153), 405–426. <https://doi.org/10.1098/rspb.1979.0006>
- Vachon, D., & Prairie, Y. T. (2013). The ecosystem size and shape dependence of gas transfer velocity versus wind speed relationships in lakes. *Canadian Journal of Fisheries and Aquatic Sciences*, 70(12), 1757–1764. <https://doi.org/10.1139/cjfas-2013-0241>
- Valiente, N., Eiler, A., Alleson, L., Andersen, T., Clayer, F., Crapart, C., et al. (2022). Catchment properties as predictors of greenhouse gas concentrations across a gradient of boreal lakes. *Frontiers in Environmental Science*, 10, 880619. <https://doi.org/10.3389/fenvs.2022.880619>
- Voigt, C., Marushchak, M. E., Mastepanov, M., Lamprecht, R. E., Christensen, T. R., Dorodnikov, M., et al. (2019). Ecosystem carbon response of an Arctic peatland to simulated permafrost thaw. *Global Change Biology*, 25(5), 1746–1764. <https://doi.org/10.1111/gcb.14574>
- Voigt, C., Virkkala, A.-M., Hould Gosselin, G., Bennett, K. A., Black, T. A., Detto, M., et al. (2023). Arctic soil methane sink increases with drier conditions and higher ecosystem respiration. *Nature Climate Change*, 13(10), 1095–1104. <https://doi.org/10.1038/s41558-023-01785-3>
- Walter, K. M., Zimov, S. A., Chanton, J. P., Verbyla, D., & Chapin, F. S. (2006). Methane bubbling from Siberian thaw lakes as a positive feedback to climate warming. *Nature*, 443(7107), 71–75. <https://doi.org/10.1038/nature05040>
- Wilson, A. G., & Izmailov, P. (2020). Bayesian deep learning and a probabilistic perspective of generalization. In H. Larochelle, M. Ranzato, R. Hadsell, M. Balcan, & H. Lin (Eds.), *Advances in neural information processing systems* (Vol. 33, pp. 4697–4708). Curran Associates, Inc.